ACS Combinatorial Science

Research Article

pubs.acs.org/acscombsci

The Different Roles of Entropy and Solubility in High Entropy Alloy Stability

Benjamin Ruiz-Yi,[†,‡] Jonathan Kenneth Bunn,[†,‡] Drew Stasak,[§] Apurva Mehta,[∥] Matthew Besser,[⊥] Matthew J. Kramer,[⊥] Ichiro Takeuchi,[§] and Jason Hattrick-Simpers*,[†,‡]

[†]Department of Chemical Engineering, University of South Carolina, Columbia, South Carolina 29208, United States

[‡]SmartState Center for the Strategic Approaches to the Generation of Electricity, University of South Carolina, Columbia, South Carolina 29208, United States

[§]Department of Materials Science and Engineering, University of Maryland, College Park, Maryland 20742, United States

[∥]Stanford Synchrotron Radiation Lightsource, SLAC National Accelerator Laboratory, Menlo Park, California 94025, United States

[⊥]Ames Laboratory, Iowa State University, Ames, Iowa 50011, United States

Supporting Information

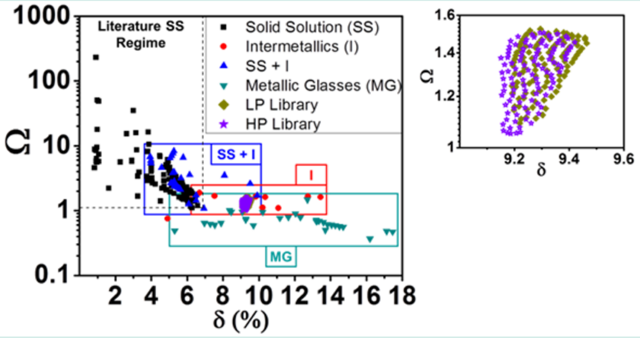

ABSTRACT: Multiprincipal element high entropy alloys stabilized as a single alloy phase represent a new material system with promising properties, such as high corrosion and creep resistance, sluggish diffusion, and high temperature tensile strength. However, the mechanism of stabilization to form single phase alloys is controversial. Early studies hypothesized that a large entropy of mixing was responsible for stabilizing the single phase; more recent work has proposed that the single-phase solid solution is the result of mutual solubility of the principal elements. Here, we demonstrate the first self-consistent study of the relative importance of these two proposed mechanisms. In situ high-throughput synchrotron diffraction studies were used to monitor the stability of the single phase alloy in thin-film $(Al_{1-x-y}Cu_xMo_y)FeNiTiVZr$ composition spread samples. Our results indicate that a metastable solid solution can be captured via the rapid quenching typical of physical vapor deposition processes, but upon annealing the solid-solution phase stability is primarily governed by mutual miscibility.

KEYWORDS: *entropy, solubility, alloys, stability, metastable solid solution, mutual miscibility*

■ INTRODUCTION

The Gibbs Phase Rule indicates that alloys containing multiple principal elements are prone to the formation of multiple complex secondary phases.[1,2] Extensive secondary phase formation can lead to materials prone to brittle fracture, reduced low-temperature toughness, and poor resistance to creep at high temperatures.[3−6] In conventional metallurgy, this has led to generations of standard alloys based on a single principal element. However, the observations of a relatively new class of materials, high entropy alloys (HEAs), demonstrated that single phase alloys can form when five or more principal constituent elements are combined in near-equiatomic proportions. HEAs form a single phase solid solution, often with a simple BCC or FCC type structure.[4,7] These alloys have been proposed to exhibit many interesting physical characteristics related to the near-random atomic environments of the constituents, often referred to as the "cocktail effect".[4,8] Such properties can include increased hardness, compressibility, microstructural stability,[9−13] reduced diffusion rates,[14] and low density.[15] In addition, HEAs have been theorized to retain properties at high temperatures, such as yield strength, elasticity, and corrosion resistance.[16−19] These alloys promise to improve performance for a range of high-temperature applications, including coatings for turbine blades, nuclear claddings, and drill bits.[20,21]

To date, however, there are open questions regarding the stabilization mechanism of these alloys. The initial hypothesis was that single phase alloy formation is driven by a large entropic contribution to the Gibbs free energy of mixing.[22,23] This contribution increases as the number of elements increase following the configurational entropy which is written as $\Delta S_{conf} = R \ln n$; where n is the number of elements and R is the gas constant.[4] The current convention in the literature is that the minimum number of elements required for an alloy to be defined as a HEA is five components with the concentrations of the elements ranging between 5 at. % and 35 at. %.[4] At sufficiently high temperature, the Gibbs free energy of mixing is lower than the Gibbs free energy of intermetallic formation,

Received: May 31, 2016
Revised: July 29, 2016
Published: August 5, 2016

DOI: 10.1021/acscombsci.6b00077
ACS Comb. Sci. 2016, 18, 596−603

despite the less negative enthalpy of mixing in comparison to the enthalpy of intermetallic formation.[22,23]

More recent work has emphasized the role of mutual solubility of the constituents in a common structure as a driving force for HEA stability. For instance, starting with the HEA forming CoCrFeMnNi base alloy, studies have explored the role of solubility by the addition of new elements (Ge or Cu) or substitution of the existing elements (e.g., V for Fe).[3,24] In both instances, the HEA solid solution was destabilized and multiple phases were observed. Zhang et al. hypothesized that secondary phase formation was related to the immiscibility of binary mixtures in the alloy. Calculation of phase diagrams (CALPHAD) studies were used to calculate binary phase diagrams of pairs in the failed alloys.[25] It was found that in the base CoCrFeMnNi alloy system, binary solubility in a FCC structure was maintained, due to the presence of elements that enhance the solubility of Cr and Mn in the base structure. However, the CALPHAD calculations showed that when additions or substitutions resulted in secondary phases, a large miscibility gap or complete insolubility was predicted in a binary phase diagram with the new element.[23] This result suggested that solubility was the primary driving factor for the stabilization of the solid-solution phase.

However, CALPHAD calculations must be extrapolated from known binary or ternary phase diagrams. In the event of partially investigated binary or ternary systems, CALPHAD can make inaccurate predictions. Furthermore, CALPHAD can only be performed on equilibrium phases, and thus cannot take into account effects from material synthesis and processing. An additional complication is that according to the entropic stabilization theory of HEAs, the solid solution phase is metastable at low temperatures.[26] This can lead to the observation of secondary phase formation in the as-synthesized samples if the quenching rate is insufficient. The criticality of the quenching rate post-heat-treatment is a well-known issue in the analogous field of bulk metallic glasses.[27,28] This can make comparisons between alloys with different constituents challenging in a single study and complicates cross-validation between studies. Therefore, studies are required that specifically target the issue of phase stability by simultaneously probing the importance of the solubility and entropic mechanisms efficiently.

High-throughput experimentation (HTE) is an established methodology for systematically probing the multiparameter spaces needed to differentiate the relative importance of the competing mechanisms. The HTE approach rapidly synthesizes hundreds of samples in a single synthesis step and then uses parallel or serial techniques to interrogate the samples for their figure of merit, in this case phase stability.[29] HTE has previously been used in the screening and discovery of ferromagnetic, piezoelectric, and optical materials.[30−32] In the field of high temperature alloys, Metting et al. used HTE to screen for transient metal and oxide phase dynamics in Ni−Al bond coats at temperatures up to 1323 K.[33] Ludwig et al. have since used a similar approach to look at phase regions of thin-film Ni−Al alloys by monitoring their electrical, optical, and mechanical properties after annealing at temperatures up to 773 K.[34] Recently, Payne et al. used ex situ XPS, EDX, and Raman studies to identify oxidation resistant alloys by monitoring low temperature oxidation of $Al_xFe_yNi_{1-x-y}$ alloys.[35] More recently, we demonstrated that in situ synchrotron diffraction can be used to track metal and oxide formation in Fe−Cr−Al alloys in a fraction of the time required for traditional bulk studies.[36] HTE studies like those listed above can provide a powerful tool for quantifying metal phase stability and are ideally suited to assess the importance of the conflicting stabilization criteria reported in the literature.

Here, we will discuss an investigation of the relative importance of the HEA stabilization mechanisms (solubility versus entropy) using thin-film continuous composition spread (CCS) samples. A series of $(Al_{1-x-y}Cu_xMo_y)$FeNiTiVZr pseudoternary thin film samples deposited at different conditions were investigated for the stability of the HEA solid solution phase. This system was chosen because the AlFeNiTiVZr, CuFeNiTiVZr, and MoFeNiTiVZr systems have been previously cited by Yeh et al. as HEAs.[4] Additionally the combined system satisfies the entropic criterion by providing enough elements and increasing the configurational entropy. It also satisfies and dissatisfies a solubility criterion that will be elaborated below. This composition contains eight principal elements in the appropriate proportions, thus satisfying the condition that n be sufficiently large for the entropic stabilization mechanism to be valid. Sputtered thin films, in fact, are an ideal test-bed for this mechanism, as the adatoms atomically mix at the substrate surface and quench at rates exceeding 1000 K/s.[37] The solubility stabilization mechanism was probed by including elemental pairs whose binary phase diagrams contain different dominant alloying structures. Aluminum and copper form a FCC binary alloy, aluminum and molybdenum form a BCC binary alloy, and copper and molybdenum are immiscible within one another. Additionally, the five common elements (Fe, Ni, Ti, V, and Zr) are able to form BCC, ordered BCC-like structures (B2), or closed packed structures.[38−40] Although not all of the elements contained in the alloy are fully miscible in one another, the criterion by Zhang et al. only requires "some" miscibility. The actual extent of solubility required is currently unclear, but here we adopt the rational that a binary so lubility of at least 5 at% is sufficient, consistent with the work of Zhang. Thus, the two mechanisms were simultaneously investigated in a well-controlled and reproducible manner and insights into the dominant mechanism were obtained. The stability of the HEA phase was determined via in situ combinatorial synchrotron diffraction studies performed from room temperature up to 733 K.

RESULTS AND DISCUSSION

Characterization of Observed Phases. Two CCS libraries were deposited at different deposition powers in order to determine effects from processing. One sample library was deposited with all targets receiving 150 W of sputter gun power and is designated as the high power (HP) sample library. The other was deposited with all targets receiving 50 W and is designated as the low power (LP) sample library. Figure 1 shows representative diffraction patterns from each of the main phases observed in the study. In all of the as-deposited samples, the films exhibited a broad peak at ~2.91 Å^{-1} likely corresponding to a single phase alloy. In the light of the fact that all data sets show only a polycrystalline diffraction peak it is difficult to make an unambiguous attribution of the peak to a particular structure. However, several heuristics point to the formation of a BCC structure. First, the base alloy would prefer a BCC structure based on their mutual solubility. Second, the valence electron concentration is less than 6.87, which Guo et al. have previously shown to favor the formation of a BCC solid solution.[41] Finally, as will be discussed below, only the BCC forming Mo−Al edge of the sample remain stable upon

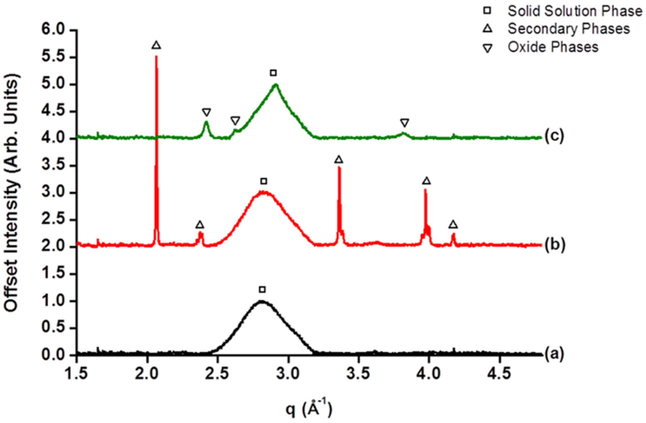

Figure 1. Synchrotron diffraction of the CCS sample. Representative diffraction patterns of the HP library are shown with (a) a single phase HEA at room temperature and (b) the same alloy exhibiting secondary phase precipitation at 733 K after annealing for 1 h. (c) The oxidized diffraction pattern is of the LP library 733 K after annealing for 1 h. The patterns have been normalized to the solid solution peak. The main HEA phase is located at 2.91 Å^{-1}. Peak shift was attributed to a change in the lattice due to the difference in compositions. □, solid solution phase; Δ, secondary phases; ▽, oxide phases. Al, 2.8 at. %; Cu, 4.8 at. %; Mo, 10.6 at. %; Fe, 17.8 at. %; Ni, 14.4 at. %; Ti, 16.3 at. %; V, 18.5 at. %; Zr, 15.0 at. %.

annealing. This peak is therefore tentatively indexed as a disordered cubic solid solution with a *d*-spacing of 2.16 Å based on a possible (110) BCC local ordering. On the basis of estimated calculations using Vegard's law from Senkov et al. and lattice constants retrieved from Materials Project, a calculated *d*-spacing value of 2.21 Å for the (110) BCC was determined.[42,43] In some regions of the CCS, multiple, sharp, intense peaks are observed and are attributed to unidentified intermetallic phases. Identification of the intermetallic phases is not the focus of this study because the presence of the phases is preferred for the analysis. The intermetallic phases are inhomogeneously distributed, as a function of composition, due to the nonequilibrium deposition process. After annealing in air for 6 h, the LP sample visibly oxidizes and a number of new peaks appear, which are attributed to unindexed oxide phases. From the Ellingham diagram for oxides, it is likely that Zr, Al, and Ti are oxidizing, although with the number of elements present in the HEA it is unlikely that the pure phase oxides are formed.[44] More detailed studies of the actual oxides formed are currently being performed.

In Situ Phase Mapping of CCS as a Function of Synthesis. Figures 2 and 3 show in situ phase stability mappings of the HP and LP $(Al_{1-x-y}Cu_xMo_y)$FeNiTiVZr alloy samples as a function of temperature, respectively. The compositions are reported in relative atomic percentage of the varying elements. In both samples the as-deposited state shows strong HEA phase formation. Depending on the deposition condition used different regions of the CCS samples show secondary phase formation. The two samples will be discussed in turn and compared below. In HP sample library, Figure 2a), the intermetallic phases are mostly clustered on the Cu−Mo edge of the CCS sample. After annealing the sample at 513 K, Figure 2b), new secondary phases emerge in the Mo heavy corner of the pseudoternary phase diagram. As temperature increases to 733 K, Figure 2c), the intermetallic peaks begin to dominate in the Mo region and are seen along the entire Cu−Mo edge of the sample. A second line of HEA

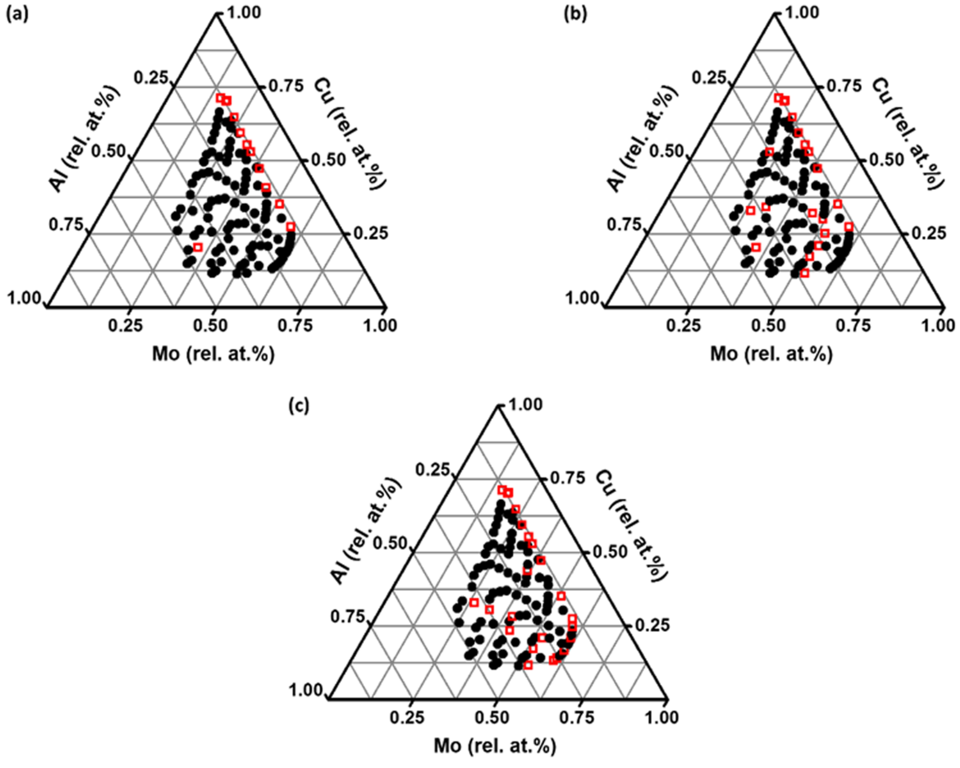

Figure 2. Pseudoternary phase diagrams of the HP $(Al_{1-x-y}Cu_xMo_y)$FeNiTiVZr alloy system. (a) shows the phase distribution in the as-deposited sample, (b) after annealing in air at 513 K, and (c) after annealing in air at 733 K. Black solid circle, single HEA phase; red open square, mixed phases.

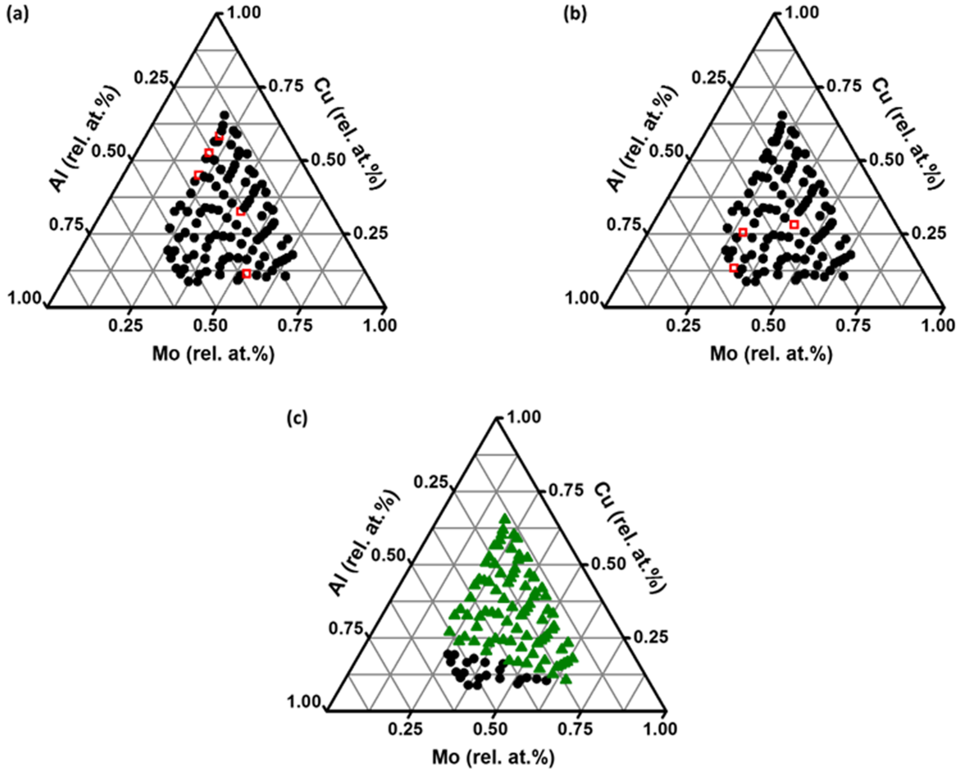

Figure 3. Pseudoternary phase diagrams of the LP $(Al_{1-x-y}Cu_xMo_y)$FeNiTiVZr alloy system. Panel a shows the as-deposited sample; panel b shows annealed in air at 598 K; and panel c shows the sample after it was annealed in air at 733 K. Black filled circle, single HEA phase; red open square, mixed phases; green filled triangle, oxidized. The total atomic percentage of FeNiTiVZr was held constant at approximately 83.3 at. %.

destabilization is also observed in the sample containing roughly 37.5 rel. at.% Al.

While the as-deposited HP library exhibits large regions of secondary phase growth, the as-deposited LP library has relatively few compositions exhibiting secondary phase growth with no strong underlying compositional trend. Figure 3a) shows three small secondary phase regions in the as-deposited film, this time concentrated along the Al−Cu binary, where a transition from a BCC to FCC structure would be expected. The large band that was seen in the Cu−Mo edge of the HP film in Figure 2a) is completely absent. After annealing at 598 K (Figure 3b), the secondary phases observed in the as-deposited films have dissolved back into the solid-solution, but three new compositions exhibit intermetallic phase formation. Figure 3c) shows the phase distribution after annealing in air at 733 K. Oxidation is observed on the sample, with only the regions containing sufficient Al remaining unoxided, indicating a possible protective Al region where oxidation is prevented. Despite the onset of oxidation, the HEA peak is still observed throughout the sample. As discussed above, the oxidation was attributed to the increased annealing time for the LP sample library.

Aluminum-Rich Composition Spread. A second set of experiments were performed on vacuum annealed samples to strengthen the argument for the formation of a solid solution phase over an amorphous phase in the CCS samples. An Al rich composition region was selected for this follow-up study as both the HP and LP libraries had shown the HEA phase to be stable in this region. Two CCS samples were synthesized with Al concentrations greater than 62.5 relative at.%, as seen in Figure 4. The samples were sputtered with the AlFeNiTiVZr target at 150 W, while the CuFeNiTiVZr and MoFeNiTiVZr targets were sputtered with 50 W gun power at 0.667 Pa Ar on 7.62 cm diameter Si wafers.

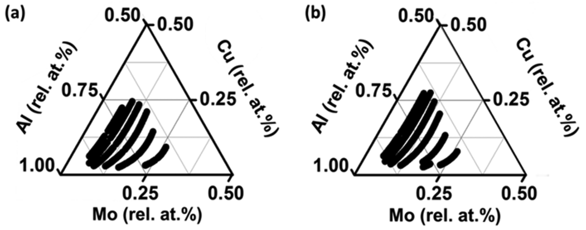

Figure 4. Pseudoternary phase diagrams of the Al rich composition spread. (a) As-deposited composition. (b) Vacuum-annealed sample spread. No secondary phase formation was observed in the analysis of either sample. The total atomic percentage of FeNiTiVZr was held constant at approximately 83.3 at. %.

Diffraction studies were performed on the as-deposited sample and on a sample that was annealed at 873 K for 6 h as seen in Figure 5. The crystallinity of the sample was measured using wide-angle X-ray scattering (WAXS) at an incidence angle of 8° and a source X-ray wavelength of 1.5418 Å with a SAXSLAB Ganesha 300 XL. The entire compositional range studied here was found to be a single phase solid solution. The fwhm of the as-deposited peak is 0.389 $Å^{-1}$ and the fwhm of the vacuum annealed sample is 0.063 $Å^{-1}$, with no secondary peaks appearing after annealing. This strongly supports the formation of a single phase solid solution structure, as opposed to a glass, since crystallization of a glass containing this number of elements would likely have resulted in multiple phases being present.[45,46]

This is the first systematic study to determine the dominant stabilizing mechanism for HEA formation. Comparing samples

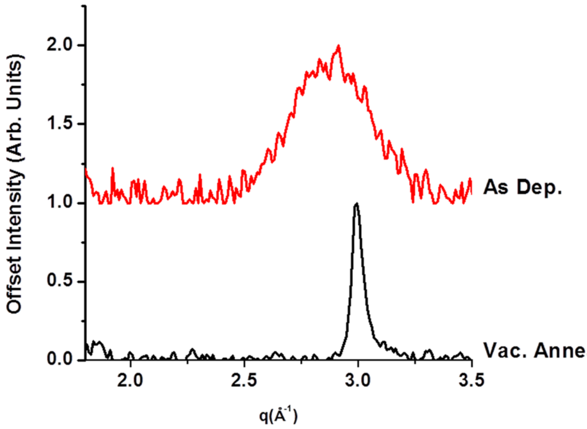

Figure 5. Characteristic diffraction of the Al-rich HEA sample at the same composition. The as deposited sample had a broad peak with a fwhm of 0.389 $Å^{-1}$. The vacuum annealed sample has a fwhm of 0.063 $Å^{-1}$. Al, 13.5 at. %; Cu, 1.7 at. %; Mo, 2.6 at. %; Fe, 17.6 at. %; Ni, 16.2 at. %; Ti, 16.7 at. %; V, 16.3 at. %; Zr, 15.5 at. %.

deposited with different overall energies illustrates that a combination of adatom energetics and quenching rate impact the ability to capture a highly unstable HEA phase across the entire pseudoternary. Upon annealing, both samples preserved the HEA single solid solution phase along the Al−Mo edge. The HP library does retain the HEA phase in the center of the phase diagram throughout the heat treatments considered in this study. On the basis of the phase diagrams, Cu prefers a FCC structure with Al placing it in competition with the BCC structure that the Al−Mo heavy composition would stabilize.[38] The presence of Mo also seems to have a destabilizing effect, which is to be expected due to its immiscibility with Cu. This agrees with observations made by Zhu et al. where the BCC structure preferred by the Al−Mo binary destabilizes the FCC in their AlCoCrCuFeNiMo$_y$ system due to the insolubility of Cu and Mo.[47] Furthermore, from Figures 2a−c), secondary phases seen on the Cu−Mo edge of the sample grow with increasing annealing temperature and eventually completely consume the regions of high Mo concentrations. A similar trend is observed in the LP library, only here the immiscibility of Cu and Mo drive oxidation during the segregation of the elements.

The ability to form a nearly complete solid solution across the entire pseudoternary, as in the LP sample library, would seem to imply that entropy can drive the formation of the solid solution phase so long as the quenching rate is sufficiently large. However, if this were the case then the HP deposition should also have exhibited nearly pure solid solution formation across the entire pseudoternary phase diagram, as this would increase the overall energy of depositing adatoms. Instead the additional energy provided to the adatoms during deposition at 150 W provided more mobility to the adatoms at the surface allowing them to settle into the more stable intermetallic phases.[48,49] This indicates that the adatoms from the LP deposition were likely quenched too rapidly to permit sufficient diffusion for the formation of equilibrium phases. This claim is strengthened by since both samples in this study showed destabilization of the HEA phase due to the addition of high concentrations of immiscible Cu and Mo. This indicates that solubility is likely a much stronger driver for HEA formation than the entropic contribution.

To provide context for this study in comparison to the literature in Figure 6, we have plotted a common measure for the ability to form a solid-solution (Ω) for a series of alloys, including those from this experiment, against the atomic size difference from Yang et al. Here, the ability of each alloy to form a solid-solution was calculated following Yang et al. using $\Omega = T_m \Delta S_{mix}/|\Delta H_{mix}|$ where T_m is the melting temperature of the compound calculated as the rule of mixtures.[50] The atomic size difference was calculated using $\delta = \sqrt{\sum_{i=1}^{N} c_i (1 - r_i/\overline{r})^2}$ where $\overline{r} = \sum_{i=1}^{N} c_i r_i$.[51] For each value all eight elements were included in the calculations and can be seen in the Supporting Information. From the figure, our samples fall into a region previously unexplored by the literature residing on the edge of a region of mixed solid solution and intermetallics, pure intermetallics and metallic glasses. We have clearly shown that the sample retains a pure HEA phase for the most Al-rich samples despite there being conflict of phase stability in the

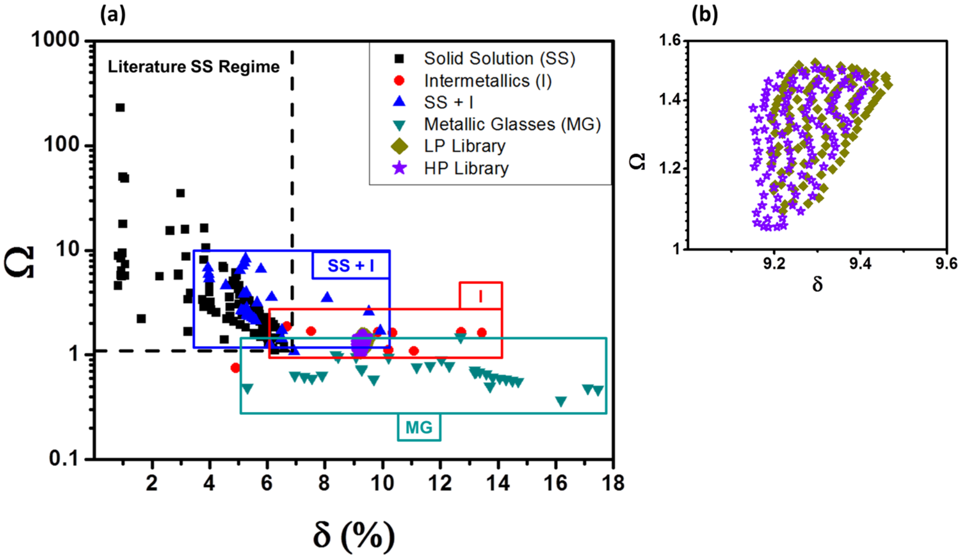

Figure 6. Solid solution formation ability and atomic size difference. (a) Comparison of Ω versus the atomic size differences of the HEA systems retrieved from literature compared to both samples.[50] (b) Zoomed in for the HP and LP sample libraries.

literature. This points to an advantage of the CCS approach in that the samples are all synthesized under exactly the same conditions and thus the difficulties of extrapolating between different synthesis conditions used by the different groups in the literature is avoided. This can provide a more definitive mapping of what phases are capable of forming HEAs, although detailed bulk studies still need to be performed to ensure the ability to "scale up" stable HEAs.

■ CONCLUSIONS

In summary, a series of HEA samples were synthesized and processed using HTE methodologies to test competing stabilization mechanisms for the formation of a single solid solution HEA phase. It was found that synthesis conditions could be identified which strongly biased the formation of an unstable BCC structure across the entire $(Al_{1-x-y}Cu_xMo_y)$-FeNiTiVZr pseudoternary system. However, upon annealing the samples, the tendency of Cu to form a FCC structure and the insolubility of the Cu−Mo binary pairing drives phase segregation, which is observed in the formation of intermetallics and oxides. While there is nonsystematic growth of secondary phases in the libraries before and after annealing that signifies metastable behavior, the retention of the major alloy peak across the CCS is representative of a dominant phase at all processing conditions. This indicates that when investigating a new HEA system, mutual solubility of elements in a common structure is the most important factor determining overall phase stability. In the future, further oxidation and microstructural studies are required to determine the role of oxygen partial pressure and microstructure on the observed HEA stability. Further studies are also under way to understand the mechanical properties of these samples such as residual deposition stress, fatigue at operating conditions, and the elastic modulus of the alloy. Additionally, selected bulk sample compositions have been synthesized via arc-melting and characterization studies are in progress.

■ EXPERIMENTAL PROCEDURES

The films were synthesized by cosputtering 99% pure AlFeNiTiVZr, CuFeNiTiVZr, and MoFeNiTiVZr alloy targets on a 7.62 cm Si substrate, resulting in an $(Al_{1-x-y}Cu_xMo_y)$FeNiTiVZr pseudoternary continuous composition spread (CCS) of an eight element assemblage. The impurities in the targets can been in the Supporting Information. Stoichiometric sputtering of the targets was confirmed by wavelength dispersive X-ray spectroscopy (WDS) measurements. For each target a series of calibration samples were deposited at 50 and 150 W at 0.667 Pa Ar on 7.62 cm diameter Si wafers. The deposition rate versus power for each target was then determined by measuring the 2D thickness profile using a Tencor Alpha-Step 200 profilometer. These measurements were used by an in-house sputter modeling software to approximate an initial pseudoternary phase compositional spread.[52]

The $(Al_{1-x-y}Cu_xMo_y)$FeNiTiVZr CCS samples were deposited onto a 7.62 cm diameter Si wafer via cosputtering of the three targets. For the CCS deposited at 150 W (HP sample library), the AlFeNiTiVZr, CuFeNiTiVZr, and MoFeNiTiVZr targets were simultaneously deposited for 48 min in a 0.667 Pa Ar atmosphere, with all materials deposited at 150 W RF, producing a thin film with an average thickness of 300 nm. For the CCS deposited at 50 W (LP sample library), the same targets were deposited for 345 min in a 0.667 Pa Ar atmosphere with all materials deposited at 50 W RF, producing a thin film with an average thickness of 500 nm. To ensure that the predicted composition spread was accurate, WDS was performed on 177 points across each sample, using pure metal standards of each element. A correction procedure was utilized due to the overlapping spectra of Ti and V. Each point provided compositions of all eight elements in the HEA. The maximum standard deviation of the experiment was 0.10 at. %. The compositions from the diffracted sample were correlated to the measured WDS composition, and used to construct the pseudoternary phase diagrams.

In situ high-temperature diffraction studies were performed at the 1−5 beamline of the Stanford Linear Accelerator Center. This facility has been described in detail previously by Gregoire et al.[53] Each CCS sample was mounted onto a substrate heater and the substrate stage was aligned with the X-ray source to have an incidence angle of 8°. The X-ray source had an energy of 15 keV (wavelength 0.82657 Å). The samples were first scanned at room temperature over a grid of 107 evenly distributed points in the as-deposited state. The samples were then heated up in air, allowed to equilibrate for 15 min and diffraction patterns were taken at the same 107 points for each annealing temperature. GI-XRD measurements were taken at room temperature, 438, 598, and 733 K for the sample deposited at 50 W conditions and at room temperature, 513 and 733 K for the sample deposited at 150 W conditions. Each wafer scan took approximately 75 min to complete with heating, equilibration, and scanning. Therefore, differences in the observed oxidation of the two samples (described below) are attributed to the difference in overall time the samples were held at temperature.

The sample to detector distance and detector tilt were calibrated using a LaB_6 standard. The 2D diffractograms were integrated along the azimuthal direction to produce 1D powder diffraction patterns using Fit2D.[54,55] A cubic spline background subtraction and normalization were performed on all patterns and the CombiView clustering analysis package was used to help identify regions exhibiting a pure solid solution phase.[56]

■ ASSOCIATED CONTENT

Ⓢ Supporting Information

The Supporting Information is available free of charge on the ACS Publications website at DOI: 10.1021/acscombsci.6b00077.

Calculated thermodynamic values related to each composition both pseudoternary phase diagrams (XLSX)

Alloy structures with atomic percentages greater than 1%[38−40] (XLSX)

Impurity elements in target material (ppm) (XLSX)

■ AUTHOR INFORMATION

Corresponding Author

*E-mail: simpers@cec.sc.edu.

Author Contributions

The manuscript was written through contributions of all authors. All authors have given approval to the final version of the manuscript.

Funding

The authors thank the Illinois Clean Coal Institute for providing funding through ICCI 15-06. The work is funded in part by the Advanced Research Projects Agency-Energy (ARPA-E), U.S. Department of Energy, under Award number DE-AR000049. We also acknowledge the support of the SmartState Center for the Strategic Approaches to the Generation of Electricity. This is supported, in part, by the Critical Materials Institute, an Energy Innovation Hub funded by the U.S. Department of Energy (DOE), Office of Energy Efficiency and Renewable Energy, Advanced Manufacturing Office. The Ames Laboratory is operated by Iowa State University under DOE Contract No. DE-AC02-07CH11358. This work made use of the South Carolina SAXS Collaborative, supported by the NSF Major Research Instrumentation program (award DMR-1428620). Use of the Stanford Synchrotron Radiation Lightsource, SLAC National Accelerator Laboratory, is supported by the US Department of Energy, Office of Science, Office of Basic Energy Services under Contract No. DE-AC02-76SF00515

Notes

The authors declare no competing financial interest.

■ REFERENCES

(1) Davis, J. R. *Metals Handbook*, Vol. *1*, 10th ed.; Davis, J. R., Ed.; ASM International: Materials Park, OH, 1990.

(2) Davis, J. R. *Metals Handbook*, Vol. 2, 10th ed.; Davis, J. R., Ed.; ASM International: Materials Park, OH, 1990.

(3) Cantor, B.; Chang, I. T. H.; Knight, P.; Vincent, A. J. B. Microstructural Development in Equiatomic Multicomponent Alloys. *Mater. Sci. Eng., A* **2004**, *375–377*, 213–218.

(4) Yeh, J.-W.; Chen, S.-K.; Lin, S.-J.; Gan, J.-Y.; Chin, T.-S.; Shun, T.-T.; Tsau, C.-H.; Chang, S.-Y. Nanostructured High-Entropy Alloys with Multiple Principal Elements: Novel Alloy Design Concepts and Outcomes. *Adv. Eng. Mater.* **2004**, *6* (5), 299–303.

(5) Miracle, D. B. High Entropy Alloys and Their Development as Structural Materials. *Mater. Sci. Technol.* **2015**, *31* (10), 1142–1147.

(6) Lasalmonie, A. Intermetallics: Why Is It so Difficult to Introduce Them in Gas Turbine Engines? *Intermetallics* **2006**, *14* (10–11), 1123–1129.

(7) Yeh, J.-W.; Lin, S.-J.; Chin, T.-S.; Gan, J.-Y.; Chen, S.-K.; Shun, T.-T.; Tsau, C.-H.; Chou, S.-Y. Formation of Simple Crystal Structures in Cu-Co-Ni-Cr-Al-Fe-Ti-V Alloys with Multiprincipal Metallic Elements. *Metall. Mater. Trans. A* **2004**, *35* (8), 2533–2536.

(8) Ranganathan, S. Alloyed Pleasures: Multimetallic Cocktails. *Curr. Sci.* **2003**, *85* (10), 1404–1406.

(9) Hsu, C.-Y.; Wang, W.-R.; Tang, W.-Y.; Chen, S.-K.; Yeh, J.-W. Microstructure and Mechanical Properties of New $AlCo_XCrFeMo_{0.5}Ni$ High-Entropy Alloys. *Adv. Eng. Mater.* **2010**, *12* (1–2), 44–49.

(10) Juan, C.-C.; Hsu, C.-Y.; Tsai, C.-W.; Wang, W.-R.; Sheu, T.-S.; Yeh, J.-W.; Chen, S.-K. On Microstructure and Mechanical Performance of $AlCoCrFeMo_{0.5}Ni_x$ High-Entropy Alloys. *Intermetallics* **2013**, *32*, 401–407.

(11) Li, B. S.; Wang, Y. P.; Ren, M. X.; Yang, C.; Fu, H. Z. Effects of Mn, Ti and V on the Microstructure and Properties of AlCrFeCoNiCu High Entropy Alloy. *Mater. Sci. Eng., A* **2008**, *498* (1–2), 482–486.

(12) Wang, Y. P.; Li, B. S.; Ren, M. X.; Yang, C.; Fu, H. Z. Microstructure and Compressive Properties of AlCrFeCoNi High Entropy Alloy. *Mater. Sci. Eng., A* **2008**, *491* (1–2), 154–158.

(13) Tung, C.-C.; Yeh, J.-W.; Shun, T.; Chen, S.-K.; Huang, Y.-S.; Chen, H.-C. On the Elemental Effect of AlCoCrCuFeNi High-Entropy Alloy System. *Mater. Lett.* **2007**, *61* (1), 1–5.

(14) Tsai, M.-H.; Yeh, J.-W.; Gan, J.-Y. Diffusion Barrier Properties of AlMoNbSiTaTiVZr High-Entropy Alloy Layer between Copper and Silicon. *Thin Solid Films* **2008**, *516* (16), 5527–5530.

(15) Youssef, K. M.; Zaddach, A. J.; Niu, C.; Irving, D. L.; Koch, C. C. A Novel Low-Density, High-Hardness, High-Entropy Alloy with Close-Packed Single-Phase Nanocrystalline Structures. *Mater. Res. Lett.* **2015**, *3*, 95.

(16) Gorr, B.; Azim, M.; Christ, H.-J.; Mueller, T.; Schliephake, D.; Heilmaier, M. Phase Equilibria, Microstructure, and High Temperature Oxidation Resistance of Novel Refractory High-Entropy Alloys. *J. Alloys Compd.* **2015**, *624*, 270–278.

(17) Hsu, C.; Yeh, J.; Chen, S.; Shun, T. Wear Resistance and High-Temperature Compression Strength of FCC $CuCoNiCrAl_{0.5}Fe$ Alloy with Boron Addition. *Metallurgical and Materials Transactions A* **2004**, *35A*, 1465–1469.

(18) Huang, P.-K.; Yeh, J.-W.; Shun, T.-T.; Chen, S.-K. Multi-Principal-Element Alloys with Improved Oxidation and Wear Resistance for Thermal Spray Coating. *Adv. Eng. Mater.* **2004**, *6* (12), 74–78.

(19) Tsai, M.-H.; Wang, C.-W.; Tsai, C.-W.; Shen, W.-J.; Yeh, J.-W.; Gan, J.-Y.; Wu, W.-W. Thermal Stability and Performance of NbSiTaTiZr High-Entropy Alloy Barrier for Copper Metallization. *J. Electrochem. Soc.* **2011**, *158* (11), H1161.

(20) Lu, Y.; Dong, Y.; Guo, S.; Jiang, L.; Kang, H.; Wang, T.; Wen, B.; Wang, Z.; Jie, J.; Cao, Z.; Ruan, H.; Li, T. A Promising New Class of High-Temperature Alloys: Eutectic High-Entropy Alloys. *Sci. Rep.* **2014**, *4*, 6200.

(21) Miracle, D. B.; Miller, J. D.; Senkov, O. N.; Woodward, C.; Uchic, M. D.; Tiley, J. Exploration and Development of High Entropy Alloys for Structural Applications. *Entropy* **2014**, *16* (1), 494–525.

(22) Li, A.; Zhang, X. Thermodynamic Analysis of the Simple Microstructure of AlCrFeNiCu High-Entropy Alloy with Multi-Principal Elements. *Acta Metall. Sin. (Engl. Lett.)* **2009**, *22* (3), 219–224.

(23) Zhang, F.; Zhang, C.; Chen, S. L.; Zhu, J.; Cao, W. S.; Kattner, U. R. An Understanding of High Entropy Alloys from Phase Diagram Calculations. *CALPHAD: Comput. Coupling Phase Diagrams Thermochem.* **2014**, *45*, 1–10.

(24) Otto, F.; Yang, Y.; Bei, H.; George, E. P. Relative Effects of Enthalpy and Entropy on the Phase Stability of Equiatomic High-Entropy Alloys. *Acta Mater.* **2013**, *61* (7), 2628–2638.

(25) Kaufman, L.; Bernstein, H. *Computer Calculation of Phase Diagrams*; Kaufman, L., Bernstein, H., Eds.; Academic Press Inc, 1970.

(26) Bechhoefer, J.; Löwen, H.; Tuckerman, L. Dynamical Mechanism for the Formation of Metastable Phases. *Phys. Rev. Lett.* **1991**, *67* (10), 1266–1269.

(27) Xu, D.; Lohwongwatana, B.; Duan, G.; Johnson, W. L.; Garland, C. Bulk Metallic Glass Formation in Binary Cu-Rich Alloy Series - $Cu_{100-x}Zr_x$ (x = 34,36,38.2,40 At.%) and Mechanical Properties of Bulk $Cu_{64}Zr_{36}$ Glass. *Acta Mater.* **2004**, *52* (9), 2621–2624.

(28) Schroers, J. Processing of Bulk Metallic Glass. *Adv. Mater.* **2010**, *22* (14), 1566–1597.

(29) Maier, W. F.; Stowe, K.; Sieg, S. Combinatorial and High-Throughput Materials Science. *Angew. Chem., Int. Ed.* **2007**, *46* (32), 6016–6067.

(30) Green, M. L.; Takeuchi, I.; Hattrick-Simpers, J. R. Applications of High Throughput (Combinatorial) Methodologies to Electronic, Magnetic, Optical, and Energy-Related Materials. *J. Appl. Phys.* **2013**, *113* (23), 231101.

(31) Zhao, J. C. Combinatorial Approaches as Effective Tools in the Study of Phase Diagrams and Composition-Structure-Property Relationships. *Prog. Mater. Sci.* **2006**, *51* (5), 557–631.

(32) Potyrailo, R. A.; Rajan, K.; Stowe, K.; Takeuchi, I.; Chisholm, B.; Lam, H. Combinatorial and High-Throughput Screening of Materials Libraries: Review of State of the Art. *ACS Comb. Sci.* **2011**, *13*, 579–633.

(33) Metting, C. J.; Bunn, J. K.; Underwood, E.; Smoak, S.; Hattrick-Simpers, J. Combinatorial Approach to Turbine Bond Coat Discovery. *ACS Comb. Sci.* **2013**, *15* (8), 419–424.

(34) Thienhaus, S.; Naujoks, D.; Pfetzing-Micklich, J.; Konig, D.; Ludwig, A. Identification of Phase Regions in Thin Films Materials Libraries by Combining Electrical, Optical and Mechanical High-Throughput Measurements: A Case Study for the System NiAl. *ACS Comb. Sci.* **2014**, *16*, 686–694.

(35) Payne, M. A.; Miller, J. B.; Gellman, A. J. High-Throughput Characterization of Early Oxidation across $Al_xFe_yNi_{1-x-y}$ Composition Space. *Corros. Sci.* **2015**, *91*, 46−57.
(36) Bunn, J. K.; Fang, R. L.; Albing, M. R.; Mehta, A.; Kramer, M. J.; Besser, M. F.; Hattrick-Simpers, J. R. A High-Throughput Investigation of Fe−Cr−Al as a Novel High-Temperature Coating for Nuclear Cladding Materials. *Nanotechnology* **2015**, *26* (27), 274003.
(37) Wasa, K.; Hayakawa, S. *Handbook of Sputter Deposition Technology*, 1st ed.; Noyes Publications: Park Ridge, NJ, 1992.
(38) Massalski, T. B.; Hiroaki, O.; Subramanian, P. R.; Kacprzak, L. *Binary Alloy Phase Diagrams*, Vol.*1*, 2nd ed.; Massalski, T. B., Hiroaki, O., Subramanian, P. R., Kacprzak, L., Eds.; ASM International: Materials Park, OH, 1990.
(39) Massalski, T. B.; Hiroaki, O.; Subramanian, P. R.; Kacprzak, L. *Binary Alloy Phase Diagrams*, Vol. *2*, 2nd ed.; Massalski, T. B., Hiroaki, O., Subramanian, P. R., Kacprzak, L., Eds.; ASM International: Materials Park, OH, 1990.
(40) Massalski, T. B.; Hiroaki, O.; Subramanian, P. R.; Kacprzak, L. *Binary Alloy Phase Diagrams*, Vol. *3*, 2nd ed.; Massalski, T. B., Hiroaki, O., Subramanian, P. R., Kacprzak, L., Eds.; ASM International: Materials Park, OH, 1990.
(41) Guo, S.; Ng, C.; Lu, J.; Liu, C. T. Effect of Valence Electron Concentration on Stability of FCC or BCC Phase in High Entropy Alloys. *J. Appl. Phys.* **2011**, *109* (10), 103505.
(42) Senkov, O. N.; Scott, J. M.; Senkova, S. V.; Miracle, D. B.; Woodward, C. F. Microstructure and Room Temperature Properties of a High-Entropy TaNbHfZrTi Alloy. *J. Alloys Compd.* **2011**, *509* (20), 6043−6048.
(43) Jain, A.; Ong, S. P.; Hautier, G.; Chen, W.; Richards, W. D.; Dacek, S.; Cholia, S.; Gunter, D.; Skinner, D.; Ceder, G.; Persson, K. A. Commentary: The Materials Project: A Materials Genome Approach to Accelerating Materials Innovation. *APL Mater.* **2013**, *1* (1), 011002.
(44) Sarrazin, P.; Galerie, A.; Fouletier, J. *Mechanisms of High Temperature Corrosion: A Kinetic Approach*; Trans Tech Publications Ltd: Stafa-Zuerich, 2008.
(45) Eckert, J.; Mattern, N.; Zinkevitch, M.; Seidel, M. Crystallization Behavoir and Phase Formation in Zr-Al-Cu-Ni Metallic Glass Containing Oxygen. *Mater. Trans., JIM* **1998**, *39* (6), 623−632.
(46) Wang, W. H.; Okada, T.; Wen, P.; Wang, X.; Pan, M. X.; Zhao, D. Q.; Utsumi, W. Effect of Pressure on Nucleation and Growth in the $Zr_{46.75}Ti_{8.25}Cu_{7.5}Ni_{10}Be_{27.5}$ Bulk Glass-Forming Alloy Investigated Using in Situ X-Ray Diffraction. *Phys. Rev. B: Condens. Matter Mater. Phys.* **2003**, *68*, 184105.
(47) Zhu, J. M.; Fu, H. M.; Zhang, H. F.; Wang, a. M.; Li, H.; Hu, Z. Q. Microstructures and Compressive Properties of Multicomponent $AlCoCrFeNiMo_x$ Alloys. *Mater. Sci. Eng., A* **2010**, *527* (26), 6975−6979.
(48) Terzini, E.; Nobile, G.; Loreti, S.; Minarini, C.; Polichetti, T.; Thilakan, P. Influences of Sputtering Power and Substrate Temperature on the Properties of RF Magnetron Sputtered Indium Tin Oxide Thin Films. *Jpn. J. Appl. Phys.* **1999**, *38*, 3448−3452.
(49) Tang, L. *Fundamentals of Nanotechnology (Hornyak, G.I., et Al.) [Book Reviews]*, 1st ed.; CRC Press: Boca Raton, FL, 2009; Vol. *3*.
(50) Yang, X.; Zhang, Y. Prediction of High-Entropy Stabilized Solid-Solution in Multi-Component Alloys. *Mater. Chem. Phys.* **2012**, *132* (2−3), 233−238.
(51) Zhang, Y.; Zhou, Y. J.; Lin, J. P.; Chen, G. L.; Liaw, P. K. Solid-Solution Phase Formation Rules for Multi-Component Alloys. *Adv. Eng. Mater.* **2008**, *10* (6), 534−538.
(52) Bunn, J. K.; Metting, C. J.; Hattrick-Simpers, J. R. A Semi-Empirical Model for Tilted-Gun Planer Magnetron Sputtering Accounting for Chimney Shadowing. *JOM* **2015**, *67* (1), 154−163.
(53) Gregoire, J. M.; Van Campen, D. G.; Miller, C. E.; Jones, R. J. R.; Suram, S. K.; Mehta, A. High-Throughput Synchrotron X-Ray Diffraction for Combinatorial Phase Mapping. *J. Synchrotron Radiat.* **2014**, *21* (6), 1262−1268.
(54) Hammersley, A. P. FIT2D: An Introduction and Overview. *ESRF Int. Rep.* **1997**, ESRF97HA02T.
(55) Hammersley, A. P.; Svensson, S. O.; Hanfland, M.; Fitch, A. N.; Hausermann, D. Two-Dimensional Detector Software: From Real Detector to Idealised Image or Two-Theta Scan. *High Pressure Res.* **1996**, *14*, 235−248.
(56) Long, C. J.; Hattrick-Simpers, J.; Murakami, M.; Srivastava, R. C.; Takeuchi, I.; Karen, V. L.; Li, X. Rapid Structural Mapping of Ternary Metallic Alloy Systems Using the Combinatorial Approach and Cluster Analysis. *Rev. Sci. Instrum.* **2007**, *78* (7), 072217.